

# Supporting Information

## Anti-freezing and Moisturizing Conductive Hydrogels for Strain Sensing and Moist-electric Generation Applications

Peng He<sup>a</sup>, Junying Wu<sup>a</sup>, Xiaofeng Pan<sup>a</sup>, Lihui Chen<sup>a\*</sup>, Kai Liu<sup>a\*</sup>, Haili Gao<sup>a</sup>,

Hui Wu<sup>a</sup>, Shilin Cao<sup>a</sup>, Liulian Huang<sup>a</sup>, Yonghao Ni<sup>a,b</sup>

<sup>a</sup> College of Material Engineering, Fujian Agriculture and Forestry University, Fuzhou  
City, Fujian Province 350002, China

<sup>b</sup> Limerick Pulp and Paper Centre, Department of Chemical Engineering, University of  
New Brunswick, Fredericton, New Brunswick E3B5A3, Canada

Corresponding author:

### **Lihui Chen**

College of Material Engineering, Fujian Agriculture and Forestry University, Fuzhou  
City, Fujian Province 350002, China.

E-mail: [fafuclh@163.com](mailto:fafuclh@163.com)

### **Kai Liu**

College of Material Engineering, Fujian Agriculture and Forestry University, Fuzhou  
City, Fujian Province 350002, China.

E-mail: [liuk1103@163.com](mailto:liuk1103@163.com)

**This section includes:**

Figure S1. High-resolution C 1s XPS spectra of dried (a) CNTs and (b) TA-CNT nanocomposites.

Figure S2. TG and DTG curves of TA, CNTs, and TA-CNT nanocomposites.

Figure S3. SEM images of (a) glycerol-PVA and (b) TCGP hydrogels.

Figure S4. Plots of storage and loss moduli ( $G'$  and  $G''$ , respectively) of glycerol-PVA and TCGP hydrogels *vs.* frequency.

Figure S5. Stress-strain curves of TCGP hydrogels with different TA-CNT contents.

Figure S6. Swelling properties of glycerol-PVA and TCGP hydrogels.

Figure S7. Conductive properties of (a) thermally healed TCGP hydrogel at room temperature and (b) TCGP hydrogel at -24 °C in a circuit composed of a LED bulb and two dry batteries (3 V).

Figure S8. Resistance changes of TCGP hydrogel upon dropping a 2 g weight on its surface.

Figure S9. Relative resistance changes of TCGP hydrogel-based sensor *vs.* strain.

Figure S10. Relative resistance changes of the TCGP hydrogel under repeated tensile loading of 30% strain for 50 cycles.

Figure S11. Optimized configuration of PVA monomer adsorbed on (a) pristine (5,5) CNTs, (b) hydrated (5,5) CNTs, (c) perfect graphene, and (d) hydrated graphene.

Figure S12. Optimized configuration of TA and PVA monomers adsorbed on (a) pristine (5,5) CNTs, (b) hydrated (5,5) CNTs, (c) perfect graphene, and (d) hydrated graphene.

Figure S13. Relative capacitance changes ( $\Delta C/C_0$ ) of TCGP hydrogel-based sensor in response to hand dorsum bending motions.

Figure S14. EMG signals associated with leg movement of a volunteer, detected by commercial Ag/AgCl electrode.

Figure S15. ECG signals of a sedated volunteer, detected by commercial Ag/AgCl electrode.

Table S1. Gaussian-fitted peak compositions of dried CNTs and TA-CNT nanocomposites.

Table S2. Compositions of TCGP hydrogels.

Table S3. Comparison of gauge factors (GFs) of TCGP hydrogel and recently reported gel-based sensors.

Table S4. Adsorption energies of PVA monomer adsorbed on the surface of carbon materials with different types of defects.

Table S5. Adsorption energies of PVA and TA monomers adsorbed on the surface of carbon materials with different types of defects.

Table S6. Comparison of electric power generation of TCGP hydrogel-based moist-electric generator and recently reported moist-electric generators.

Movie S1. Comparison of dispersion behavior in solution of CNTs and TA-CNT nanocomposites.

Movie S2. Stretching behavior of TCGP hydrogel in a circuit composed of a LED bulb and two dry batteries (3 V).

Movie S3. EMG signals induced by shank bending motion, detected using the TCGP

hydrogel electrodes.

Movie S4. Process of electric power generation from moisture of TCGP hydrogel moist-electric generator.

### **Scanning electron microscopy (SEM) analysis.**

First, the glycerol in TCGP hydrogel was removed by immersing TCGP hydrogel in distilled water for 12 hours. Then, TCGP and PVA hydrogels were placed in a freeze dryer for 48 hours. The morphologies of TCGP and PVA hydrogels were observed by SEM (Thermoscientific Verios G4 UC).

### **C 1s XPS spectra of CNTs and TA-CNT nanocomposites.**

The chemical compositions of CNTs and TA-CNT nanocomposites were measured by an X-ray photoelectron spectrometer (XPS, Thermo Scientific ESCALAB 250Xi).

### **Thermogravimetric analysis (TGA).**

The thermogravimetric analysis of TA, CNTs, and TA-CNT nanocomposites were carried out on a DSC-TGA instrument (SDT Q600, TA Instruments, USA). The samples were heated from 25 to 600 °C at a heating rate of 20 °C min<sup>-1</sup> under nitrogen flow.

### **Zeta potential measurement.**

The zeta potentials of the neat CNTs and TA-CNTs nanocomposite suspensions were measured by a Malvern zeta sizer Nano ZS90 (UK).

### **Investigation of conductive properties of TCGP and thermally healed TCGP hydrogels.**

The TCGP hydrogel (2 cm length × 1 cm width × 0.5 cm thickness) was used as a conductor in a circuit to light up a LED bulb with a constant voltage of 3 V. In addition,

the TCGP hydrogel with the same size was cut into two pieces from middle and then reassembled with a hot knife. The damaged TCGP hydrogel was placed at -30 °C for 10 min to obtain the thermally healed hydrogel. Finally, the conductive properties of the thermally healed hydrogel were investigated using the above circuit.

The conductivities of glycerol-PVA and TCGP hydrogels were measured by an electrochemical workstation (Zahner, Zennium40715). The conductivity was calculated by the equation:<sup>1</sup>

$$\sigma = d/(R \times S) \quad (S1)$$

Where  $\sigma$ ,  $R$ ,  $d$ , and  $S$  are the conductivity (S.m<sup>-1</sup>), the resistance ( $\Omega$ ), the thickness (cm), and the cross-sectional area (cm<sup>2</sup>) of the hydrogel sample, respectively.

### **Swelling behaviors of TCGP hydrogel.**

The swelling behavior tests were carried out by immersing the as-prepared TCGP and glycerol-PVA hydrogels in distilled water at room temperature. The samples were taken out at regular intervals, and the moistures on the sample surface were removed with filter paper. The weights of the sample were measured. The swelling ratios ( $S$ ) were calculated as follows:

$$S = (W_s - W_d) / W_d \quad (S2)$$

Where  $W_s$  is the weight of the swollen hydrogel and  $W_d$  is the initial weight of the original hydrogel.

### **Rheological characterization analysis.**

Rheological behaviors of glycerol-PVA and TCGP hydrogels (0.5 cm length  $\times$  0.5 cm width  $\times$  0.5 cm thickness) were analyzed by a MARS III HAAKE rheometer

(Thermo Scientific, Germany) with a 35 mm parallel plate system. Dynamic frequency sweep tests were carried out from 0.01 to 10 Hz with a fixed oscillatory strain of 1% at 25 °C. The storage and loss moduli ( $G'$  and  $G''$ , respectively) of TCGP and glycerol-PVA hydrogels were tested at frequency of 1.0 Hz and strain of 1%.

### **Mechanical properties of TCGP hydrogel.**

Tensile tests of TCGP hydrogel were carried out using a digital tensile machine (KJ-1065B, Kejian Instrument Co. Ltd, China) with a 200 N load cell at a loading rate of 50 mm/min. Prior to the measurement, the TCGP hydrogels with different TA-CNT contents were cut into strips (50 mm length  $\times$  9 mm width  $\times$  4.5 mm thickness). The composition of TCGP hydrogel was listed in Table S1.

The tensile stress ( $\sigma$ ) was calculated by the following equation:

$$\sigma = F/S \quad (S3)$$

Where  $F$  is the force and  $S$  is the cross-sectional area.

The tensile strain was estimated as  $H/H_0$ , where  $H$  and  $H_0$  are the deformed height and original height, respectively.

### **Computational methods**

To understand the details of the molecular interactions between TA, PVA, and CNTs, we have performed the first-principle calculations using the DMol<sup>3</sup> program in Materials Studio<sup>2,3</sup>. The exchange-correlation function was treated by the generalized gradient approximation (GGA) with the PW91 parameterization<sup>4</sup>. We have used OBS method for DFT-D correction to refine noncovalent interaction such as hydrogen

bonding<sup>5</sup>. All systems were fully relaxed with symmetry. All-electron treatment and double numerical basis including d- and p-polarization function (DNP)<sup>1</sup> were used. The relaxation of atomic positions was considered to be converged when the change in total energy is less than  $1.0 \times 10^{-5}$  Ha/Å, and the force on each atom less than 0.002 Ha/Å.

### **Structural models**

Since the diameter of multi-wall carbon nanotubes (CNTs) used in the experiment is larger than 10 nm and TA molecule is small, the CNTs can be approximately seen as flat surfaces. Thus, it is appropriate to choose graphene as structural models to investigate the interaction between big tubular CNTs and organic molecules. To consider the curvature effect, (5,5) CNTs were employed to study the stable configurations of TA and PVA monomers on CNTs surfaces. Hydrated CNTs surfaces were simulated with two hydroxyl groups attached on the surface of pristine (5,5) CNTs or graphene (Figure S9 (b) and (d)). Stone-Wale defect was also introduced on the surface of carbon materials to investigate the influence of imperfect carbon surfaces on the structure of TCGP hydrogel.

### **Adsorption energy**

The stability of CNTs, TA, and PVA composite system can be described by the adsorption energy  $E_a$  of the molecules, which was defined as:

$$E_a = E_{\text{com}} - (E_{m1} + E_{m2} + \dots + E_{mn}) \quad (\text{S4})$$

where  $E_{\text{com}}$  is the total energies of the composite system, and  $E_{m1}$ ,  $E_{m2}$ , and  $E_{mn}$  are the

total energies of the first, second, and  $n_{\text{th}}$  molecules, respectively. For example, the adsorption energies of TA and PVA monomers on CNTs surfaces are the energy difference of total energy of the composite and components. The negative value of binding energy indicated the formation of composite system was exothermic.

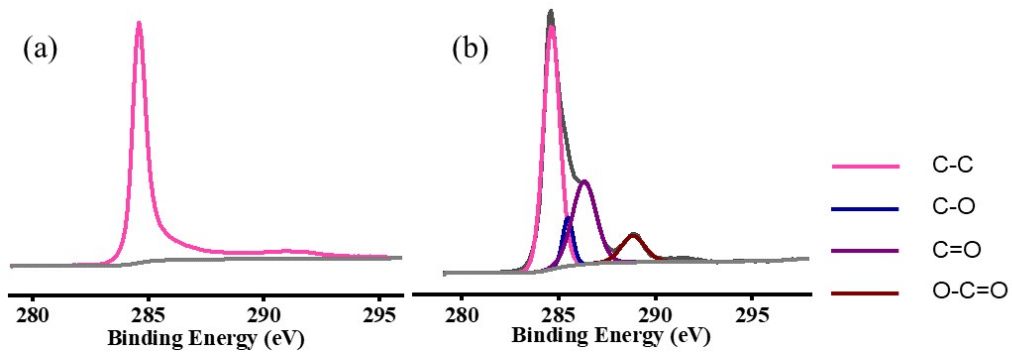


Figure S1. High-resolution C 1s XPS spectra of dried (a) CNTs and (b) TA-CNT nanocomposites.

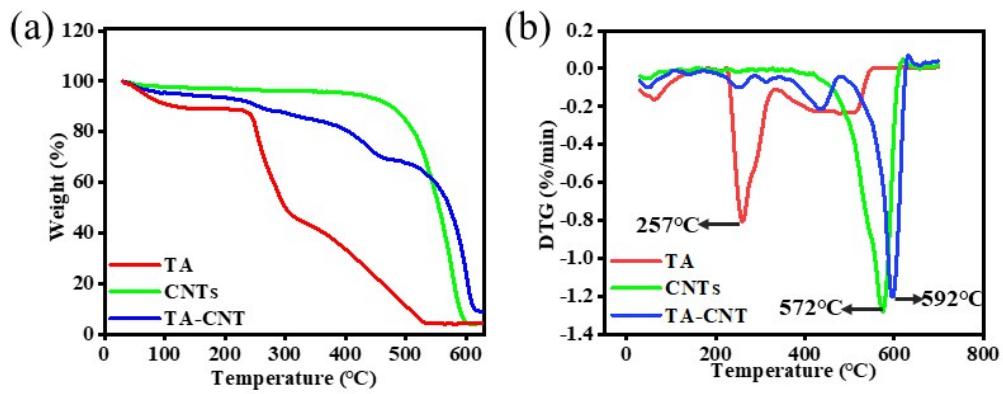


Figure S2. TG and DTG curves of TA, CNTs, and TA-CNT nanocomposites.

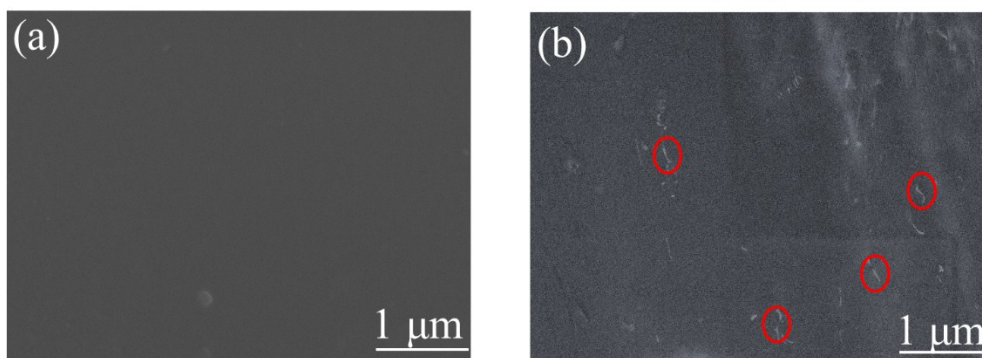


Figure S3. SEM images of (a) glycerol-PVA and (b) TCGP hydrogels.

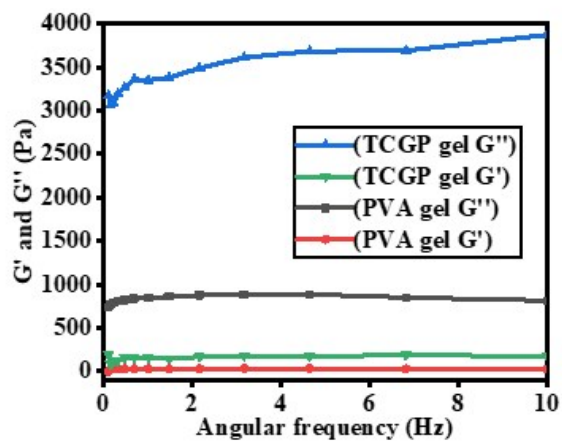


Figure S4. Plots of storage and loss moduli ( $G'$  and  $G''$ , respectively) of glycerol-PVA and TCGP hydrogels vs. frequency.

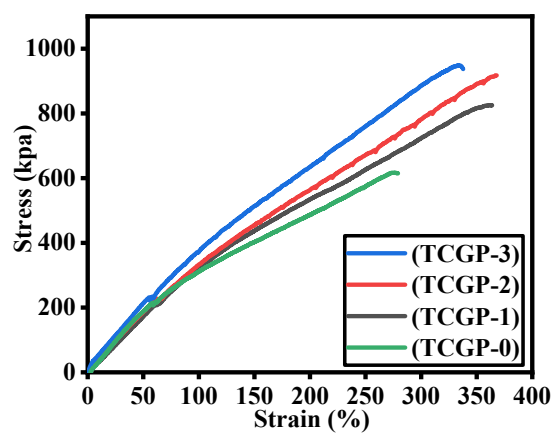


Figure S5. Stress-strain curves of TCGP hydrogels with different TA-CNT contents.



Figure S6. Swelling properties of glycerol-PVA and TCGP hydrogels.

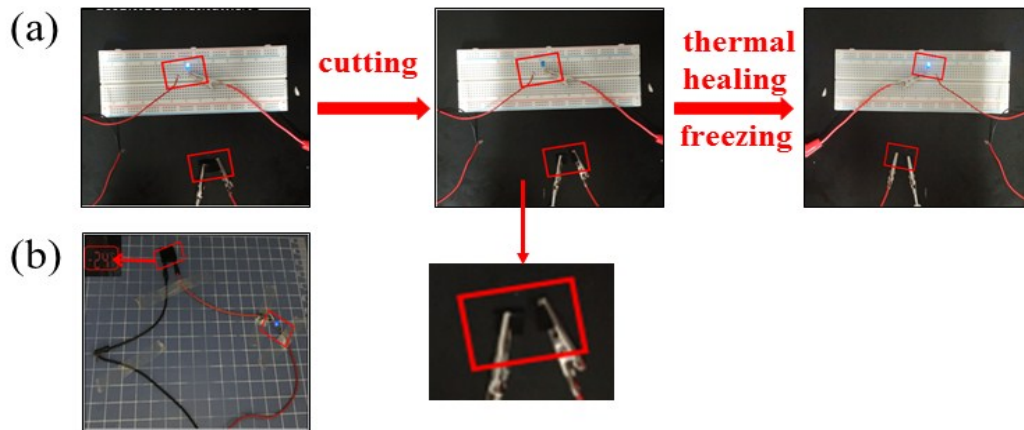


Figure S7. Conductive properties of (a) thermally healed TCGP hydrogel at room temperature and (b) TCGP hydrogel at  $-24\text{ }^{\circ}\text{C}$  in a circuit composed of a LED bulb and two dry batteries (3 V).

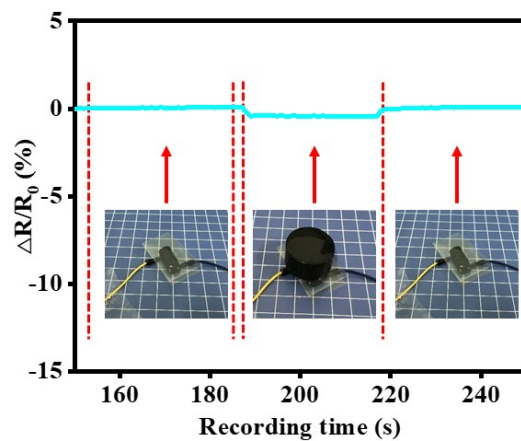


Figure S8. Resistance changes of TCGP hydrogel upon dropping a 2 g weight on its surface.

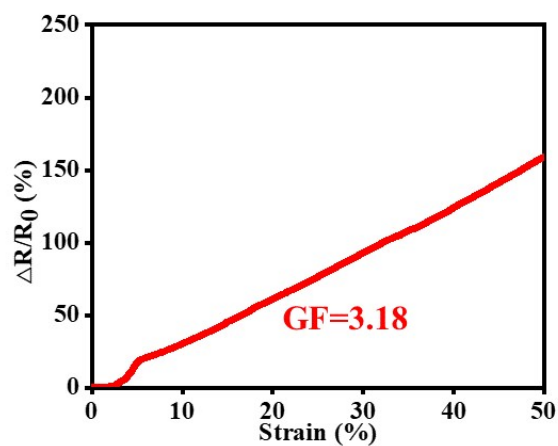


Figure S9. Relative resistance changes of TCGP hydrogel-based sensor vs. strain.

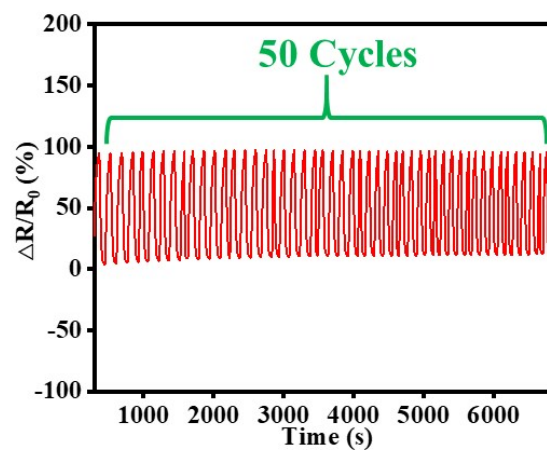


Figure S10. Relative resistance changes of the TCGP hydrogel under repeated tensile loading of 30% strain for 50 cycles.

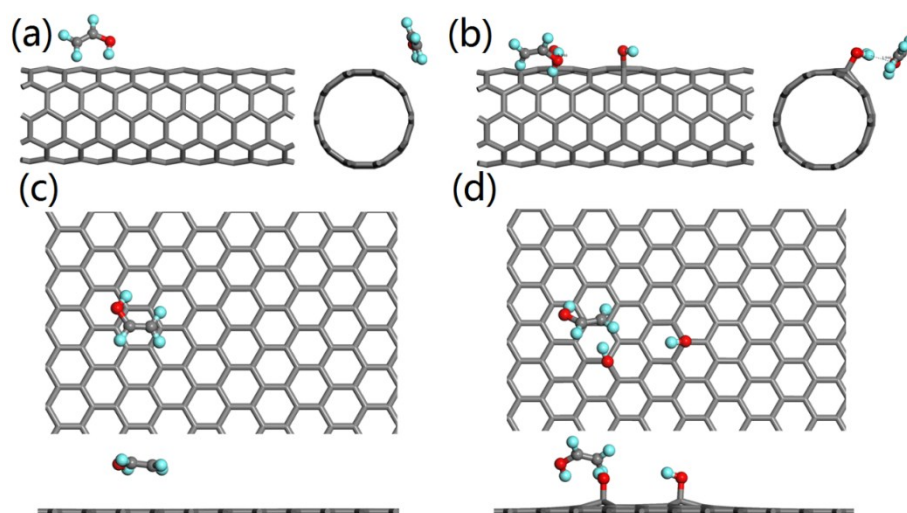


Figure S11. Optimized configuration of PVA monomer adsorbed on (a) pristine (5,5) CNTs, (b) hydrated (5,5) CNTs, (c) perfect graphene, and (d) hydrated graphene. The grey, red, and light blue spheres represent C, O, and H atoms, respectively.

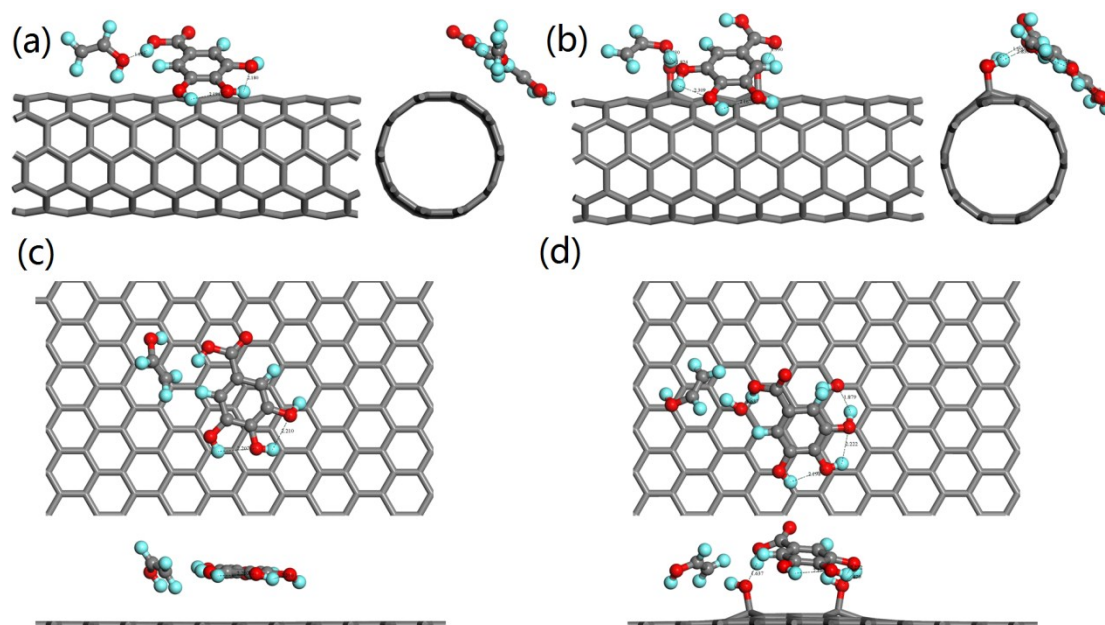


Figure S12. Optimized configuration of TA and PVA monomers adsorbed on (a) pristine (5,5) CNTs, (b) hydrated (5,5) CNTs, (c) perfect graphene, and (d) hydrated graphene. The grey, red, and light blue spheres represent C, O, and H atoms, respectively.

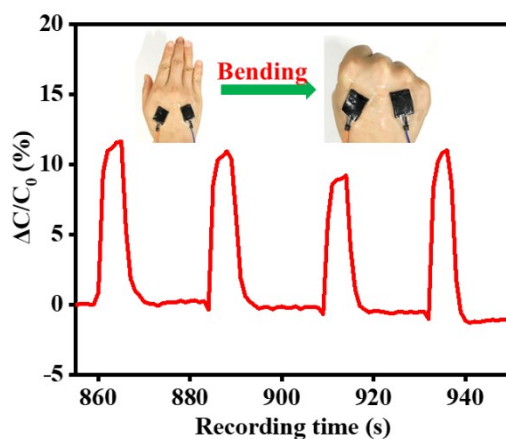


Figure S13. Relative capacitance changes ( $\Delta C/C_0$ ) of TCGP hydrogel-based sensor in response to hand dorsum bending motions.

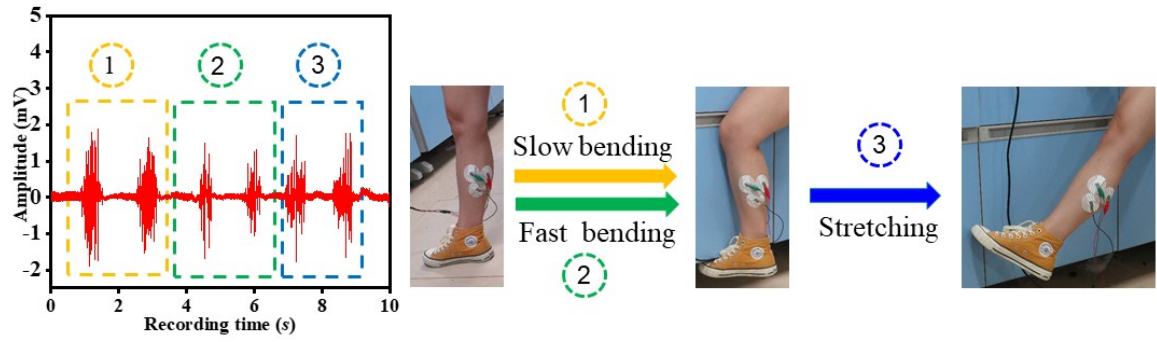


Figure S14. EMG signals associated with leg movement of a volunteer, detected by commercial Ag/AgCl electrode.

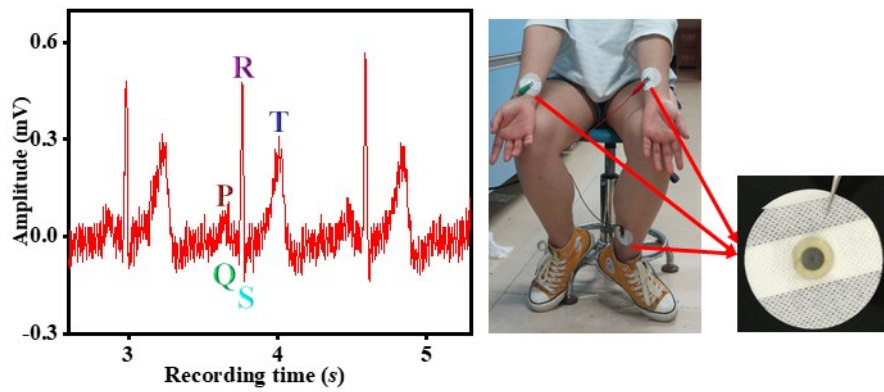


Figure S15. ECG signals of a sedated volunteer, detected by commercial Ag/AgCl electrode.

Table S1. Gaussian-fitted peak compositions of dried CNTs and TA-CNT nanocomposites.

Functional group	Binding energy (eV)	CNTs (%)	TA-CNT (%)
C-C (H)	284.6	49.12	22.1
C-O	285.5	-	2.76
C=O	287.4	-	10.98
O-C=O	288.9	-	3.46

Table S2. Compositions of TCGP hydrogels.

	CNTs (g)	TA (mg)	Glycerol (mL)	H <sub>2</sub> O (mL)	PVA (g)
TCGP-0	-	-	10	10	3.25
TCGP-1	0.1	50	10	10	3.25
TCGP-2	0.2	100	10	10	3.25
TCGP-3	0.3	150	10	10	3.25

Table S3. Comparison of gauge factors (GFs) of TCGP hydrogel and recently reported gel-based sensors.

Material	Conductive component	Gauge factor (tensile strain)	Reference
PVA	Carbon nanotube	1.51 (1000%)	S6
PVA/Polyvinylpyrrolidon e	Fe <sup>3+</sup>	0.478 (200%)	S7
PAAm	LiCl	0.84 (40%)	S8
PAA	rGO/Fe <sup>3+</sup>	1.32 (500%)	S9
<b>PVA</b>	<b>TA/CNT</b>	<b>3.18 (50%)</b>	<b>This work</b>

Table S4. Adsorption energies of PVA monomer adsorbed on the surface of carbon materials with different types of defects.

Adsorbed molecule	PVA monomer		
Carbon materials	Pure (eV)	Stone-Wale (eV)	-OH (eV)
(5,5) CNT	-0.461	-0.460	-0.550
Graphene	-0.403	-0.569	-0.807

Table S5. Adsorption energies of PVA and TA monomers adsorbed on the surface of carbon materials with different types of defects.

Adsorbed molecule PVA and TA monomers			
Carbon materials	Pure (eV)	Stone-Wale (eV)	-OH (eV)
(5,5) CNT	-1.780	-1.775	-2.106
Graphene	-2.171	-2.199	-2.555

Table S6. Comparison of electric power generation of TCGP hydrogel-based moist-electric generator and recently reported moist-electric generators.

Material	Voltage (mV)	Electric-generation mechanism	Reference
Porous carbon film	68	Proton movement	[S10]
Silk cocoon membrane	31	Ions transport	[S11]
PPy skeleton	60	Ions movement	[S12]
PPy nanowire	72	Ions movement	[S13]
Graphene oxide nanoribbons	40	Proton transport	[S14]
<b>TCGP hydrogel</b>	<b>80</b>	<b>Proton transport</b>	<b>This work</b>

## References

- S1. J. Han, H. Wang, Y. Yue, C. Mei, J. Chen, C. Huang, Q. Wu, X. Xu, Carbon 149 (2019) 1-18.
- S2. B. Delley, J. Chem. Phys. 92(1990) 508-517.
- S3. B. Delley, J. Chem. Phys. 113(2000) 7756-7764.
- S4. J.P. Perdew, Y. Wang, Phys. Rev. B 45(1992) 13244-13249.
- S5. F. Ortmann, F. Bechstedt, W.G. Schmidt, Phys. Rev. B 73 (2006) 205101.
- S6. G. Cai, J. Wang, K. Qian, J. Chen, S. Li, P.S. Lee, Advanced Science 4 (2017) 1600190.
- S7. Y.-J. Liu, W.-T. Cao, M.-G. Ma, P. Wan, ACS Applied Materials & Interfaces 9 (2017) 25559-25570.
- S8. K. Tian, J. Bae, S.E. Bakarich, C. Yang, R.D. Gately, G.M. Spinks, M. in het Panhuis, Z. Suo, J.J. Vlassak, Advanced Materials 29 (2017) 1604827.
- S9. X. Jing, H.-Y. Mi, X.-F. Peng, L.-S. Turng, Carbon 136 (2018) 63-72.
- S10. K. Liu, P. Yang, S. Li, J. Li, T. Ding, G. Xue, Q. Chen, G. Feng, J. Zhou, Angew. Chem. Int. Ed. 2016, 55, 8003.
- S11. B. Tulachan, S. K. Meena, R. K. Rai, C. Mallick, T. S. Kusurkar, A. K. Teotia, N. K. Sethy, K. Bhargava, S. Bhattacharya, A. Kumar, R. K. Sharma, N. Sinha, S. K. Singh, M. Das, Sci. Rep. 2014, 4, 5434.

S12. J. Xue, F. Zhao, C. Hu, Y. Zhao, H. Luo, L. Dai and L. Qu, *Adv. Funct. Mater.*, 2016, 26, 8784.

S13. X. Nie, B. Ji, N. Chen, Y. Liang, Q. Han and L. Qu, *Nano Energy*, 2018, 46, 297.

S14. F. Zhao, L. Wang, Y. Zhao, L. Qu, L. Dai, *Advanced Materials*, 2017, 29, 1604972.